



Mechanical and Tribological Properties of MgO/ Multiwalled Carbon Nanotube-Reinforced Zirconia-Toughened Alumina Composites Developed through Spark Plasma Sintering and Microwave Sintering

K. L. Meena, Ch. S. Vidyasagar, and D. Benny Karunakar

Submitted: 7 September 2020 / Revised: 27 July 2021 / Accepted: 13 August 2021 / Published online: 13 October 2021

Nanoceramic composites exhibit superior properties over their microcounterparts due to their microstructural differences. However, achieving grain size reduction in these composites through grain suppression is limited. Therefore, the use of nanopowders (both matrix and reinforcement) at the starting level itself and an attempt to further reduce the grain size may yield extraordinary properties. Thus, the present research aims to investigate the tribological and mechanical properties of ZTA nanocomposites reinforced with nano-MgO/MWCNT. The composites were developed separately through spark plasma sintering (SPS) and microwave sintering. The experimental results showed that with increase in the normal load and sliding velocity, the COF decreases, while the wear rate increases. Further, both the COF and wear rate increased with increase in the normal load and sliding velocity beyond a certain point. Moreover, when the normal load is increased beyond 65N, the wear rate of the composites increases rapidly irrespective of the sliding velocities. The addition of MgO increased the hardness through a secondary phase and pinning effect of the composites, while the addition of MWCNTs increased their fracture toughness through crack branching. The wear rate and the COF of the SPS composites were better than their MW-sintered counterparts.

Keywords coefficient of friction, microwave sintering, multiwalled carbon nanotubes (MWCNTs), spark plasma sintering, wear rate, zirconia-toughened alumina

1. Introduction

Removal of material from the surface of a member in relative motion with another member or members due to rubbing and mating is called wear. Sudden failures create many doubts about the reliability of the component and hence limit the development of new machines (Ref 1). Therefore, control of wear becomes essential for manufacturers to produce high-quality and durable wear-resistant material. However, the rate of wear is based on working conditions and varies with material type. Moreover, it should be noted that wear is usage of material and not its property (Ref 2, 3).

In past few decades, the number of studies targeting the development of alumina-zirconia composites with enhanced mechanical and tribological properties has increased exponentially (Ref 4, 5). At present, ZTA ceramics, classified as new generation ceramics, are popular as they exhibit remarkably higher (4 times) fracture toughness compared to alumina alone

(Ref 6). Initially, the main objective of zirconia's addition to alumina was to improve its density. However, later, zirconia was found to be a potential reinforcing material to improve the fracture toughness of alumina (Ref 7, 8). However, like any other material, these ceramic composites also possess certain drawbacks and suffer from issues like corrosion and oxidation at both normal and high temperatures. Besides, ceramics like ZrO_2 and Al_2O_3 do not have these drawbacks, but they become brittle on trying to improve their strength and so lose their applicability. However, the low cost of zirconia and alumina makes them attractive to the designers and manufacturers for use in various applications despite their inferior mechanical properties as compared to other ceramics like nitrides and carbides. The important properties of alumina like hardness, fracture toughness, flexural strength, and wear resistance can be improved by reinforcing with zirconia (Ref 9-12).

The addition of small amounts of MgO up to 1.0 wt.% promotes the pinning effect in the ZTA matrix and hence improves the wear and overall mechanical properties (Ref 13-16). By varying the amount of MgO addition in the range of 0-1 wt.% to 3 mol.% Y stabilized ZTA, high-strength insert tools were developed and are promising to replace carbide or coated carbide inserts in the future (Ref 17-19). The occurrence of phase transformation in the zirconia-alumina composites enhanced their wear performance on comparison with composites of monolithic alumina (Ref 20). Cao et al., (Ref 21) confirmed that reinforcing CNT to ZTA enhanced the density, microhardness, fracture toughness and flexural strength where 0.1 wt.% CNT reinforcement exhibited peak results by suppressing the growth of grains in the matrix. Azhar et al., (Ref 22) developed ZTA composites reinforced with MgO and found the increase in hardness of the cutting insert is mainly

K. L. Meena, Ch. S. Vidyasagar, and D. Benny Karunakar,
Department of Mechanical and Industrial Engineering, Indian Institute
of Technology Roorkee, Roorkee, Uttarakhand 247667, India. Contact
e-mail: kmeena@me.iit.ac.in.

contributed by small-sized Al_2O_3 grains. For dental applications, Zhang et al. (Ref 23) reinforced varying amounts of Alumina in the range of 0.25-2.5 wt.% to 2-3 mol.% yttria-stabilized polycrystal (TZP) and investigated their low-temperature degradation. Rittidech et al., (Ref 24) investigated the influence of 1-8 wt.% Y_2O_3 addition on the phase formation and fracture toughness of the developed $\text{Al}_2\text{O}_3 - x\text{ZrO}_2 - \text{Y}_2\text{O}_3$ (AZY) ceramics and concluded that addition of Y_2O_3 does not affect the shape of grains in the AZY matrix. Melk et al. (Ref 25) reported a decrease in the COF and wear rate of 2 wt.% MWCNT reinforced 3Y-TZP under lower load conditions. Mazumder et al., (Ref 26) concluded that the COF of CuO-reinforced 3Y-TZP decreased by 38% when compared to pure 3Y-TZP due to the formation of protective tribofilm on the substrate. Ghosh et al. (Ref 27) obtained a low COF and specific wear rate at elevated temperature in 3Y-TZP composites by reinforcing with 0.5 wt.% of MgO and 6 wt.% of Mo due to formation of MoO_3 phase. Dilshad et al. (Ref 28) improved the hardness and fracture toughness of ZTA- CeO_2 composites by achieving the formation of $\text{LaAl}_{11}\text{O}_{18}$ phase in the matrix by reinforcing with 3 wt.% of La_2O_3 . Kuntz et al. (Ref 29) reported improved hardness, fracture toughness and wear performance in ZTA matrix composite reinforced with 0.5 wt.% of Cr_2O_3 .

It is a known fact that nanoceramic composites exhibit superior properties over their microcounterparts. However, achieving grain size reduction in these composites through grain refinement is limited. Therefore, the use of nanopowders (both matrix and reinforcement) at the starting level itself and then attempt to further reduce the grain size by grain refinement may yield extraordinary results. After performing a critical review of the open literature, it was observed that the effects of various additives on the mechanical and wear properties of ZTA composites were evaluated at the microlevel. Further, very limited studies reported the use of nanoadditives like MgO and MWCNTs to develop ZTA composites. Moreover, the development of these composites at the nanoscale (both matrix and reinforcement) is rarely reported. Therefore, the present study focuses on the development of nano-ZTA composites by reinforcing nano-MgO and MWCNTs separately to nanoalumina and consolidates them through SPS and MWS and evaluates their mechanical and tribological properties.

2. Experimental Procedures

2.1 Starting Materials

Powders of MgO (99% purity, 3.58 g/cm^3 theoretical density and 40 nm average particles size), MWCNTs (97% purity, 8-15 layer, 12-15 nm of outer diameter, 0.5-5 μm in length, $231.85 \text{ m}^2/\text{g}$ of surface area, and 2.6 g/cm^3 theoretical density) and 99% purity 3mol% yttria-stabilized zirconia (3YSZ) having an average particle size of 40 nm with monoclinic phase were used as reinforcement materials. Commercially available 99% purity $\alpha\text{-Al}_2\text{O}_3$ nanopowder with an average particle size of 100 nm used as matrix material was procured from 'Nano Partech', India.

2.2 Composite Development

The procedure and steps taken for production of present nanocomposites start with blending MgO and MWCNTs

separately to alumina-zirconia matrix and consolidating the resulting mixtures separately through SPS and MWS processes. Four separate ceramic composite samples were sintered through MWS- and SPS-based on the elemental percentages shown in Table 1.

Two different compositions, namely 1 vol.% MgO + 10 vol.% $\text{ZrO}_2 + \text{Al}_2\text{O}_3$ and 1 vol.% MWCNTs + 10 vol.% $\text{ZrO}_2 + \text{Al}_2\text{O}_3$, were sintered separately through SPS and MWS respectively. The starting powders were separately weighed conforming to the amounts presented in Table 1. The powders were blended manually in an agate mortar using a pestle for 40 min. Poly vinyl alcohol (PVA) was used to temporarily bind the powders together during blending. The binder helps to hold the powder particles together when they are pressed into the required shape as the green preforms are very delicate and difficult to handle. The blended composite powders were dried at 50°C for removing any moisture present before sieving to remove agglomerated lumps and impurities. For microwave sintering, a customized vacuum furnace with a 1.5 kW power supply ('Omicron Scientific Equipment Company, Dwarka, New Delhi, India') was used. The variations in the sample temperature were measured through an infrared thermometer which focused on the surface through a small hole provided on the sintering chamber. In MWS, the compacts were placed on a SiC susceptor, which is a hybrid conductor and then the susceptor along with the samples is placed in the MW furnace at a frequency of 2.45 GHz. From room temperature, the furnace temperature is gradually increased to the desired sintering temperature and held their short period time before cooling down. The detailed parameters employed here are given in Table 2. On the other hand, an SPS furnace (Dr. Sinter, SPS-625 Japan) was used to consolidate the composite powders. An optical pyrometer focused on the surface of graphite die was used to measure the sintering temperature. A dilatometer was used to record and store the shrinking rate and related parameters such as pressure, temperature, voltage, and current. In SPS, the powder sample was poured into a graphite die and the graphite punches were inserted from both ends. The die punch assembly was placed into the sintering chamber with appropriate graphite spacers. The sintering cycle was carried out through a preset computer program written according to the parameters shown in Table 2. The temperature was increased from room temperature to a fixed sintering temperature at a fixed rate of temperature rise and, after the holding time, allowed to cool. In both the sintering cases, the sintered samples were 3-mm-thick circular tablets with a diameter of 15 mm. Process parameters of both MWS and SPS are given in Table 2.

Zirconia-toughened alumina (ZTA) tends to react with MWCNTs; more significantly its effect is on formation of secondary phases. Thus, the mechanical property enhancement results are directly from the secondary phases particles (Ref 30). However, for CNT-ceramic nanocomposites, the major challenges are CNT agglomeration, insufficient densification at high CNT content and low interfacial adhesion between CNTs and ceramics. High-temperature sintering has a detrimental effect on CNTs (Ref 31). To prevent the degradation of CNTs, SPS is an ideal consolidation technique effectively preventing grain growth and preserving the integrity of the delicate structures of the carbon allotrope reinforcements. SPS presents several advantages, including relatively low sintering temperatures, shorter sintering periods, high densification and high heating and cooling rates. MWS processes require high

Table 1 Selected composites for investigating the tribological properties

Developed composite	MgO, vol. %	MWCNTs, vol. %	ZrO ₂ , vol. %	Al ₂ O ₃ , vol. %	Sintering temp, °C
MgO-ZTA through SPS	1	0	10	89	1300
MgO-ZTA through MWS	1	0	10	89	1300
MWCNT-ZTA through SPS	0	1	10	89	1500
MWCNT-ZTA through MWS	0	1	10	89	1500

Table 2 Parameters of MWS and SPS processes used in the present study

Parameter	MWS process	SPS process
Pressure	100 MPa (Hydraulic Pressure)	60 MPa (Constant)
Sintering temperature	1500°C	1300°C
Heating rate	25°C/min	100°C/min
Holding time	20 min	5 min
Sintering environment	Inert gas (Argon gas)	Vacuum

sintering temperatures to achieve sufficient densification when compared to SPS process (Ref 32).

2.3 Characterization

The samples were prepared for the microstructure examination by first polishing them on various SiC grade papers and cloth polishing until the samples were mirror polish. The mirror-polished samples were chemically etched by H₃PO₄ acid at 250°C for 2 min and gradually cooled (Ref 33). The etched samples were then observed under FE-SEM. The samples were gold-coated before the FE-SEM examination as they are non-conductive in nature. The 'Image J' software with a linear intercept approach program was used to calculate the average grain sizes of the composites using their corresponding microstructures. To evaluate the mechanical properties, microhardness and fracture tests were conducted. The microhardness was measured by a computerized Vickers hardness tester with 300-gram indenter load held for 10 seconds. For each sample, ten indentations across the area of the sample were measured for accuracy and precision. The calculated *c/a* ratio in the present work was higher than 2.5, and hence, it comes under the radial-median crack system, as stated in our previous work (Ref 34, 35). Also, under this condition, the Anstis equation is applied to calculate the fracture toughness of the samples. The Anstis equation shown in (Eq 1) (Ref 36) was used to calculate the fracture toughness (*K_{IC}*) of the composite samples.

$$K_{IC} = 0.016 \left(\frac{E}{H_V} \right)^{\frac{1}{2}} \frac{P}{c^{\frac{3}{2}}} \quad (\text{Eq 1})$$

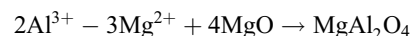
where *E* is Young's modulus of the composite, *H_v* is the micro-Vickers hardness, *P* is the indenter load, *c* is the radially measured crack length, and *a* is the half of the intended diagonal.

2.4 Conventional Oxide Mixing (Solid-Solid Reaction) Mechanisms

The formations of various secondary phases were formed by conventional oxide mixing (solid-solid reaction) with addition

of MWCNTs and MgO-reinforced ZTA composites. The present solid powders do not react together at room temperature over normal time scales, and it is necessary to heat them to much higher temperatures, often to 1000-1500°C, in order for the reaction to occur at an appreciable rate (Ref 37). It has already been discussed about the formation of secondary phase of MgAl₂O₄ with composition of MgO and Al₂O₃ by exothermic chemical reaction leading to the formation of phases. The crystallographic structure of the MgAl₂O₄ spinel is simple cubic with eight formula units in one cubic unit cell. The structure of MgAl₂O₄ was first determined by Bragg and Nishikawa independently (Ref 38, 39). The pressing of Al₂O₃ and MgO into certain shapes and then heating at high temperature for a prolonged period. The mechanism of spinel formation in this process involves a counter diffusion process that depends on a number of factors. At the beginning stage of MgAl₂O₄ formation reaction, small crystals of spinel stoichiometry are nucleated on either MgO or Al₂O₃ grains. After the formation of this initial layer, subsequent growth and thickening of spinel layer become difficult, due to the reactants now separated by an impassable spinel layer (Ref 40, 41). So a counter diffusion process takes place; Mg²⁺ ions diffuse away and Al³⁺ ions diffuse toward MgO-MgAl₂O₄ interface. Likewise, Al³⁺ ions diffuse away and Mg²⁺ ions diffuse toward MgAl₂O₄-Al₂O₃ interface (Ref 39) forming MgAl₂O₄ from oxide reactants by counter diffusion in solid oxide reaction process. The electroneutrality during the reaction is preserved due to diffusion of 3 Mg²⁺ ions for diffusion every 2 Al³⁺ ions. The reactions that occur at MgO-MgAl₂O₄ and MgAl₂O₄-Al₂O₃ interface are stated below (Ref 42):

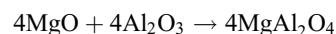
At MgO-MgAl₂O₄ interface:



At MgAl₂O₄-Al₂O₃ interface:



The overall reaction:



2.5 Tribological Studies

Wear testing of the developed composites was done on a pin-on-disk setup. The values of variables used for the calculation of COF and rate of wear are shown in Table 3. Under dry sliding conditions, the selection of certain fixed parameters like sliding distance, and varying parameters like the velocity of sliding and the normal load were done considering the values at which the samples exhibited actual sign of wear occurrence. The samples not showing any significant signs of wear below the values were selected in this work. Generally, according to the wear mechanism, the COF value remains constant after an initial fluctuation (Ref 43). However, the duration of surface contact between the pin and the disk was kept constant throughout the testing and other corresponding parameters were set according to the duration of surface contact.

The pin-on-disk apparatus comprises a pin (3 mm long and 15 mm dia) having a spherical surface at the point of contact and is placed perpendicularly to a circular rotating disk. In the present study, the pin slides about 1500 m on a circular track of 100 mm diameter for 10 minutes, where the sliding velocity remains constant. The pin was fixed perpendicularly to the disk using a holder, and the EN30 steel disk pasted with 320 grade SiC emery paper was allowed to rotate, causing the pin to wear off in a constant circular path. For each test run, completely dry abrasive grit papers were used and replaced after every 250 m sliding distance so that fresh abrasive grit was exposed to the sample specimen, and weight loss was calculated accordingly (Ref 44). The required normal load on the pin was applied by adding or removing the weights on the arm provided within the setup. The whole pin-on-disk setup was connected to a computer which provided results and graphs through the data acquisition system. The COF and rate of wear of the samples were estimated through Eq 3 and 4, respectively, as shown below (Ref 45).

$$\text{Specific wear rate } (W_s) = (\nabla V / FXL) \quad (\text{Eq 3})$$

$$\text{Coefficient of friction } (\mu) = (f / N) \quad (\text{Eq 4})$$

where ' ∇V ' is the loss of volume due to wear, which is calculated by mass loss (before test weight–after test weight),

' f ' is the frictional force, ' μ ' is the COF, ' L ' is the sliding distance, and ' N ' is the normal load.

3. Results and Discussion

3.1 XRD Analysis

The XRD phase analysis is carried out for the as-received 3 mol.% yttria-stabilized zirconia powder as well as developed ZTA composites-reinforced MgO/MWCNTs through SPS and MWS. Evaluation of the phases formed in the as-received and developed composites was done through XRD analysis, and the corresponding XRD patterns are shown in Fig. 1.

During SPS sintering, due to rapid heat and pressure being applied at the same time, the large fraction of finer t-ZrO₂ crystallites compared to the monoclinic phase were preserved leading to enhanced densification. The monoclinic phase was completely changed into tetragonal due to stabilization of zirconia with 3 mol.% yttria. Initially, in the starting nanopowder, zirconia was present in both tetragonal (high-intensity peaks of t-ZrO₂) and monoclinic (some minor peaks of m-ZrO₂) form as observed from Fig. 1(a). Figure 1(B) shows various XRD patterns of the developed composites.

Figure 1(b) (a) and (b) shows the peaks of MgO-ZTA composites sintered through SPS and MWS, respectively. It can be noticed that the major peaks indicate t-ZrO₂, α -Al₂O₃, and MgO phases, while the minor peaks indicate the secondary phase MgAl₂O₄. The lower intensities of the secondary phase peaks indicate that the degree of involvement of the secondary phase is little. Figure 1(c) and (d) shows the peaks of MWCNT-ZTA composites sintered through SPS and MWS, respectively. It can be observed that the major peaks indicate α -Al₂O₃, t-ZrO₂, MWCNTs, and the minor peaks indicating the secondary phase such as C₆Al₂O₁₂, ZrC, ZrAl₃C₄, Zr₂Al₃ in the SPS sample and C₆Al₂O₁₂, Al₂OC, ZrC in the MWS were observed. The formation of secondary phases has affected the microstructure and properties of the developed composites. The transformation of stable zirconia from t-ZrO₂ to m-ZrO₂ can be attributed to the stress-induced in composites. The high reactivity of Al₂O₃ and ZrO₂ tend to react with MWCNTs more significantly affecting formation of secondary phases and removing the problem agglomeration of MWCNTs at elevated sintering temperatures; which could inhibit the abnormal grain

Table 3 Parameters used in the present study for tribological investigations

S. no.	Parameters	Operating conditions
1	Normal load	35 N, 45 N, 55 N, 65 N, 75 N, 85 N and 95 N
2	Sliding velocity	0.79 m/s, 1.4 m/s, 1.8 m/s and 2.4 m/s
3	Disk material	EN30 steel, 62 HRC (Standard hardness)
4	Pin materials	Developed ceramic composite samples
5	Surface condition	Dry
6	Duration of rubbing	10 min
7	Sliding distance	1500 m

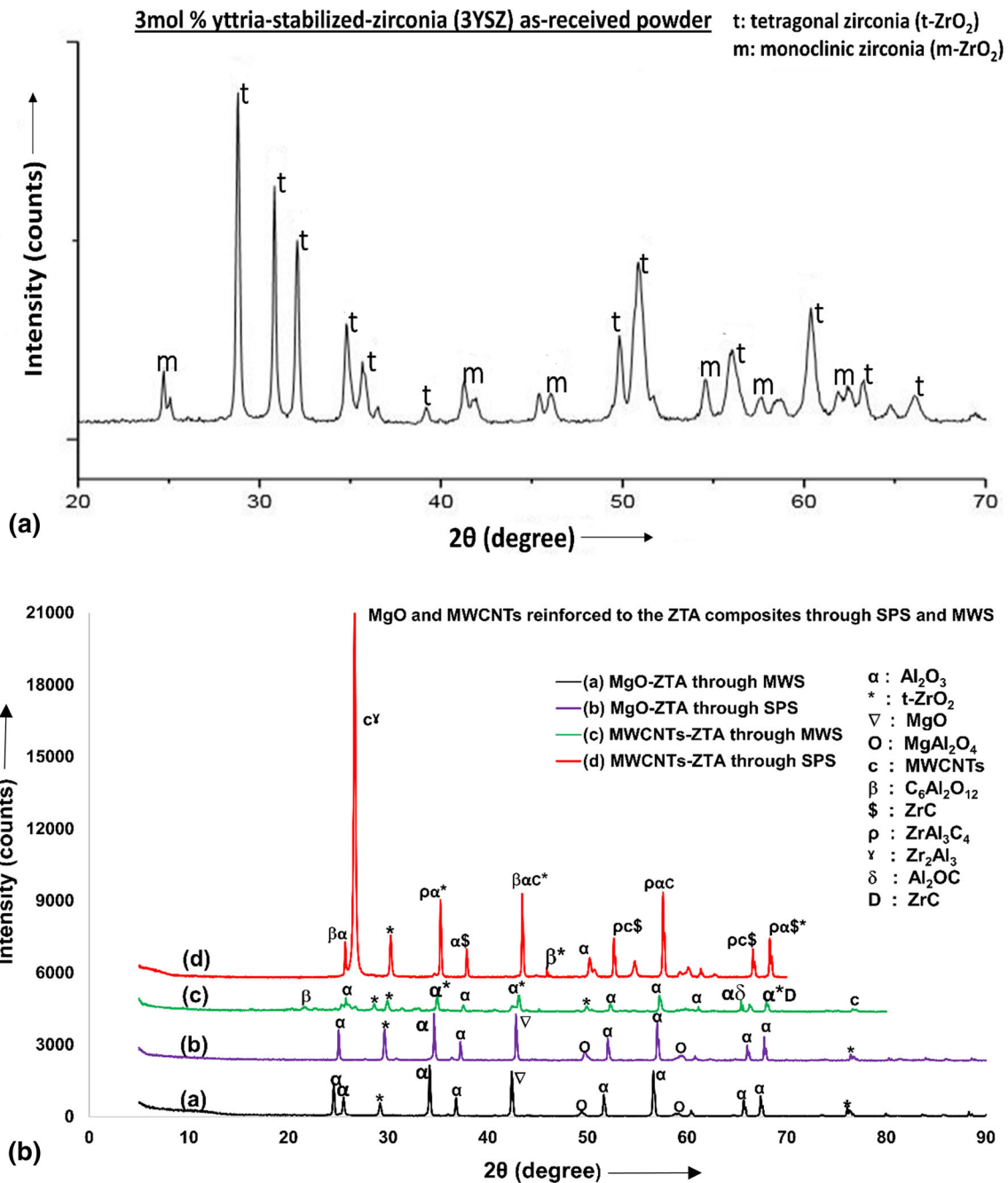


Fig. 1 XRD patterns showing (A) Peak intensities of starting 3 mol.% yttria-stabilized zirconia nano powder, (B) Developed composites (a) MgO-ZTA through MWS, (b) MgO-ZTA through SPS, (c) MWCNT-ZTA through MWS and (d) MWCNT-ZTA through SPS

growth in the Al₂O₃ matrix. Thus, the mechanical property enhancement results directly from the secondary phases particles (Ref 21).

3.2 Microstructure

Figure 2 shows the FE-SEM microstructures of the composites.

Figure 2(a) and (c) shows the microstructures of the composites sintered through SPS. It can be observed that the reinforced particles are uniformly distributed in the matrix; grains are closely packed in the matrix showing signs of grain suppression. Figure 2(b) and (d) shows the microstructures of

the composites sintered through MWS. The uniformity in distribution of the reinforced particles is observed; however, the suppression of grain growth was not as much as found in the SPS composites despite the use of higher temperature and holding time. However, from Fig. 2(a), (b), (c), and (d), it can be observed that all the developed composites exhibited uniformly dispersed MgO and MWCNTs and ZrO₂ in the alumina matrix. The formations of the secondary phase of MgAl₂O₄ show improved properties of developed composites. It is called spinel, and its cubic shape is shown in Fig. 2(a) and (b).

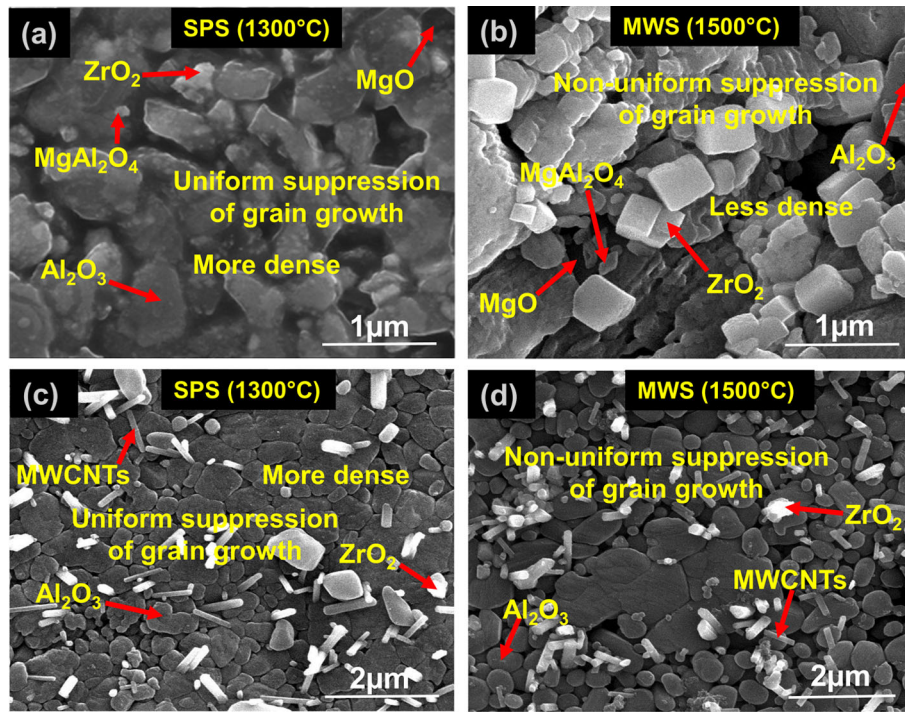


Fig. 2 FE-SEM microstructures of different composites with (a) MgO-ZTA through SPS, (b) MgO-ZTA through MWS, (c) MWCNT-ZTA through SPS and (d) MWCNT-ZTA through MWS

Table 4 The properties of developed MgO-ZTA and MWCNT-ZTA composites like relative density, average grain size, microhardness and fracture toughness

S. no.	Developed composites	Relative density, %	Average grain size, μm	Microhardness, GPa	Fracture toughness, $\text{MPa m}^{1/2}$
1	MgO-ZTA through SPS	99.68 \pm 0.11	0.380 \pm 0.04	19.56 \pm 0.17	6.7 \pm 0.84
2	MgO-ZTA through MWS	97.79 \pm 0.13	0.495 \pm 0.03	18.19 \pm 0.14	6.6 \pm 0.89
3	MWCNT-ZTA through SPS	97.80 \pm 0.15	0.311 \pm 0.05	17.75 \pm 0.13	8.5 \pm 0.95
4	MWCNT-ZTA through MWS	97.35 \pm 0.17	0.385 \pm 0.03	16.41 \pm 0.11	8.1 \pm 0.97

3.3 Average Grain Size

The grain size average was calculated through 'Image J' software as discussed earlier and is presented in Table 4. During the SPS, the powder particles get rapidly heated due to Joule's heating mechanism and alongside a high pressure being applied (Ref 46, 47), whereas in the MWS process rapid heat is applied without the use of pressure. Clearly, the SPS process, due to its unique working principle and mechanism, is better than MWS as the microstructures of the SPS processed composites are dense and show smaller grain due to grain suppression. One of the main advantages of SPS is it can offer rapid heating rates and does not allow sufficient time for recrystallization and grain growth; hence, densely packed smaller grains were achieved in the matrix. On the other hand, in MW sintering, the powders are first compacted and sintering done later; separately without applying any pressure. In comparison, SPS composites possessed better and smaller grain sizes than the MWS composites. The addition of 10 vol.% of ZrO₂ to the alumina matrix is found to be the optimum amount from our previous study (Ref 48) which could provide the highest stability of tetragonal zirconia phase within the α -alumina matrix having uniform distribution (Ref 22).

3.4 Microhardness

Table 4 shows the microhardness of the developed composites. It is noticed from Table 4 that the MgO-ZTA composites samples developed through SPS possess higher values of microhardness compared to MWS composites. It is also observed that the addition of MWCNT marginally decreased the hardness of the MWCNT-ZTA composites, while the MgO-ZTA composites exhibit comparatively higher hardness. The addition of MgO leads to the formation of a secondary phase (MgAl₂O₄), inhibiting the abnormal grain growth in the Al₂O₃ matrix, thereby increasing the hardness (Ref 34, 49).

3.5 Fracture Toughness

Table 4 also shows the variation in the fracture toughness of the composites. In SPS process, it was obtained rapidly by application of pressure within a short time as compared to MWS as discussed earlier. In SPS composites, the transformation toughening of ZrO₂ has resulted in an increase in the tetragonal phase and a decrease in the monoclinic phase as observed in Fig. 1 and is the main reason for the improved

fracture toughness in the SPS composites and it was enhanced by the formation of the secondary phases with the addition of MgO and MWCNTs within the ZTA matrix. The secondary phases caused significant and dominant pinning effect work to suppress grain growth and led to higher fracture toughness (Ref 50). Among all composites, the highest fracture toughness was seen in the MWCNT-ZTA composite developed through SPS.

3.6 Tribological Properties

All the developed composites were subjected to wear testing to evaluate the tribological properties such as the COF and rate of wear. The parameters like normal loads (N) and sliding velocities (m/s) were varied between 35 and 95 N and 0.8 and 2.4 m/s, while the sliding distance was kept constant at 1.5 km.

(a) COF variation

Figure 3 shows the effect of normal load and sliding velocity variation on the composite's COF.

From Fig. 3, it is evident that for all sliding velocities, the corresponding COF decreases with increase in the normal load. Thus, the COF decreased when normal applied load was increased and sliding velocity was decreased: more the sliding velocity, lower the COF. During wear, due to the rubbing action between the disk and pin, a tribo-layer is formed which results in a decrease in the COF. Particularly, at higher normal loads, the COF decreases further as the tribo-layer is shifted to the pin surface from the disk surface (Ref 51). Rockwell hardness C scale (HRC) of developed composites (pin) a maximum value of 83 HRC (MgO-ZTA through SPS) and a minimum value of 80 HRC (MWCNT-ZTA through MWS), which is higher than the counter disk (62 HRC, EN 30 steel). However, the counter disk was pasted with 320 grade SiC emery paper and was allowed to rotate, causing the pin to wear off (hardness of SiC

particles on the emery paper is greater than the pin) in a constant circular path.

In the SPS process, results obtained were superior to results obtained by MWS process as SPS sintered samples obtained full density and higher hardness compared to MW-sintered samples. On increase in hardness, the resistance to wear also increases. Moreover, due to the SPS conditions, a highly adhered layer formed at the contact surface, unlike the MW sintered samples because of high density resulting in the reduction of their COF. Composites sintered through SPS exhibited lower COF than MWS composites. The reinforcement of MgO promoted the pinning effect in the ZTA matrix as discussed earlier, leading to the suppression of grain growth and hence improves the hardness property of the MgO-ZTA ceramic composites (Ref 26). On the other hand, the reinforcement of MWCNTs reduced the propagation of crack by giving away to crack branching (Ref 26) leading to an improvement in the fracture toughness of the MWCNT-ZTA ceramic composites. Thus, composites reinforced with MgO exhibited lesser COF as compared to the composites reinforced with CNT as seen from Fig. 3.

Figure 4 shows the effect on COF varying with higher normal loads along with fixed sliding velocity 2.4 m/s velocity and with varying higher sliding velocities and with constant normal load.

The most influential parameter for the flash temperature rise within the specific contact was found to be sliding velocity. At higher sliding velocities and higher normal loads, the contact pressure on the asperity tip increases at the contact surface and the contact temperature rises to the flashpoint temperature of the composite allowing the wear transition to take place leading to orient deformation. An increase in COF between the pin and the disk was seen as the normal load and sliding velocities are increased to higher levels. This phenomenon led to wear transition and rapid deformation of the asperity tip in a

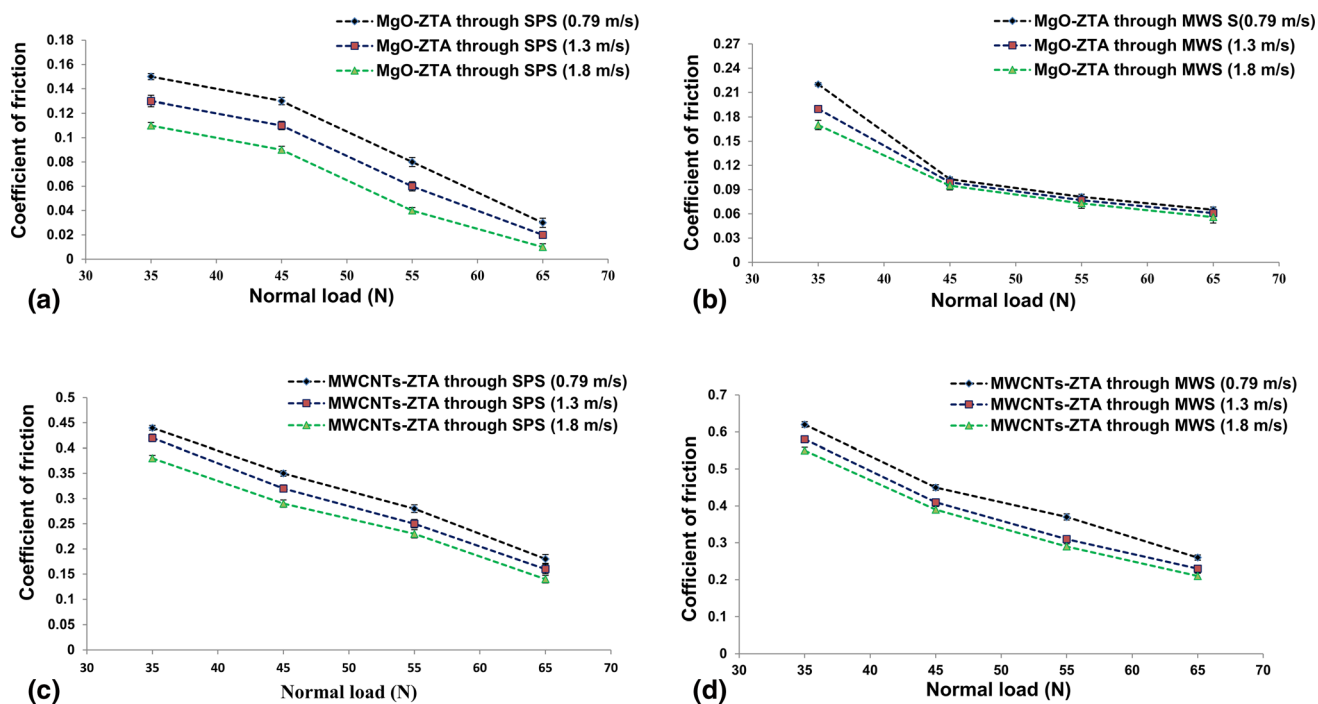


Fig. 3 Change in the COF with the variation of normal loads and sliding velocities (a) MgO-ZTA through SPS, (b) MgO-ZTA through MWS, (c) MWCNT-ZTA through SPS, (d) MWCNT-ZTA through MWS

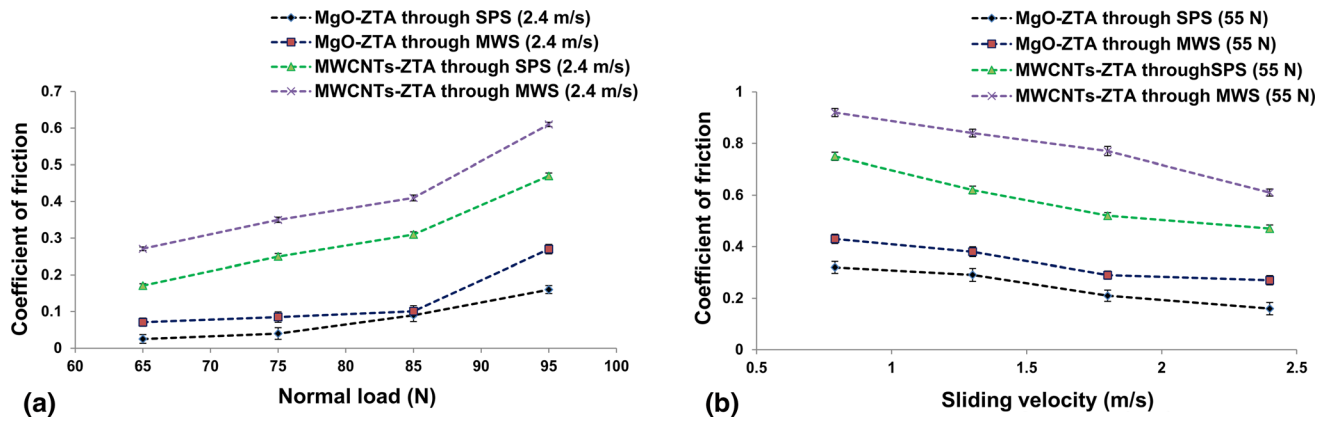


Fig. 4 Variations in the COF with (a) increase in normal load at constant sliding velocity (2.4 m/s), (b) varying sliding velocities along with constant normal load (55 N) of developed composites and comparisons between four samples

particular orientation (Ref 52). The contact of the tribological surface was found in severe wear condition due to rapid crack propagation. As discussed earlier, when the sliding velocity is increased to 2.4 m/s as seen in Fig. 4(a), the tribo-layer at the contact undergoes severe plastic deformation and ultimately breaks down (Ref 22). The composites sintered through SPS exhibited lower COF values as compared to the MWS composites. Besides, composites reinforced with MgO have shown lower COF values than the composites reinforced with MWCNTs as seen from Fig. 4(a). From Fig. 4(b), it can be seen that the COF of the composites reduced with increase in the sliding velocity and at a fixed normal load of 55 N. The values of COF of the SPS composites were found lower than those of MWS composites. The rough surface of the pin got removed at a higher sliding velocity, and a compact oxide tribo-layer started to form between the pin and disk. The SPS samples provided tribo-layers, which had higher amount of adhering to the contact surface unlike the MWS samples leading to a decrease in the COF. Accordingly, the MW sintered samples loosely adhered to tribo-layers on the surface of both the pin and disk that was worn-out quickly increasing the COF as compared to other samples. Among all the composites, the composites reinforced with MgO showed lower COF values when compared to the composites reinforced with MWCNT as observed from Fig. 4(b).

(b) Wear rate variation

The effects of normal load and sliding velocity variation on the wear rate of the composites are shown in Fig. 5.

With an increase in the normal load and sliding velocity, an increase in the wear rate of the composites was observed. Figure 5 shows that as the normal load increases, the wear rate of the composites also increases, while the wear rate decreases with an increase in the sliding velocity. At lower normal loads and sliding velocities, the removal wear is not found, so the tribo-layer formation was not observed and this can be attributed to the increased wear rate of the composites at lower loading conditions. However, as a result of the tribo-layer formation, with an increase in the sliding speed, the increase in the wear rate is gradual and progressive. This tribo-layer is a product of the environmental reaction and gets transferred from the disk to the pin during the rubbing action. The MW sintered samples have lesser adherent layer at the surface of contact that

gets removed in a shorter rubbing period, and hence, the wear rate increased. The bonding strength in grain particles in MW-sintered sample lesser than in SPS-sintered samples. Thus, the SPS sintered samples were observed to have a lower wear rate. The developed MgO-ZTA composite samples have shown a lower value of wear rate compared to the MWCNT-ZTA composites as seen in Fig. 5(a), (b), (c) and (d).

Figure 6 shows the effect on wear rate varying with higher normal loads along with fixed sliding velocity of 2.4 m/s velocity and varying higher sliding velocities along with constant normal load.

When the normal loads and velocities are higher, the contact pressure on the asperity tip at the contact surface increased and gave rise to flash temperatures allowing the wear transition and orient deformation of the asperity tips at elevated temperatures. As also discussed earlier, during rubbing, the wear was found on the contact surface or tip with deep and wide grooves resulting in crack propagation. Therefore, at higher sliding velocities and normal loads, the wear rate increases. Further, from Fig. 6(a), it can be observed that at a constant sliding velocity of 2.4 m/s, when the load is increased beyond 65 N, there is a rapid increase in the wear rate. At higher sliding velocities, very high flash temperatures are generated at the tip of the pin resulting in breakdown of the tribo-layer formed on it. Due to this, the contact area between the pin and the rubbing surface increases and therefore results in a rapid increase in the wear rate. When a tribological surface exhibits rapid crack propagation due to particles activated by wear, the surface is considered to be in severe wear. Typically, wear transition occurs suddenly from the plastic deformation to micro-crack or micro-fracture. The tribo-layer is formed on the pin by oxidation from the environment and the material that gets shifted from the rotating disk during motion. Further, the direct contact between the two surfaces in motion (pin and disk) is minimized by tribo-layer, hence reducing the wear rate of the composites. Less wear rate in the SPS composites compared to the MWS composites can be attributed to the tribo-layers adhering densely to the pin during rubbing. The MW sintered composites have loose layers between the pin and the disk that wear off rapidly, increasing the wear rate. Compared to MW-sintered samples, the composites sintered through SPS were found to have lower wear rates. Among the developed composites, the MgO-ZTA composites showed lower wear rates compared to those of the MWCNT-ZTA composites as

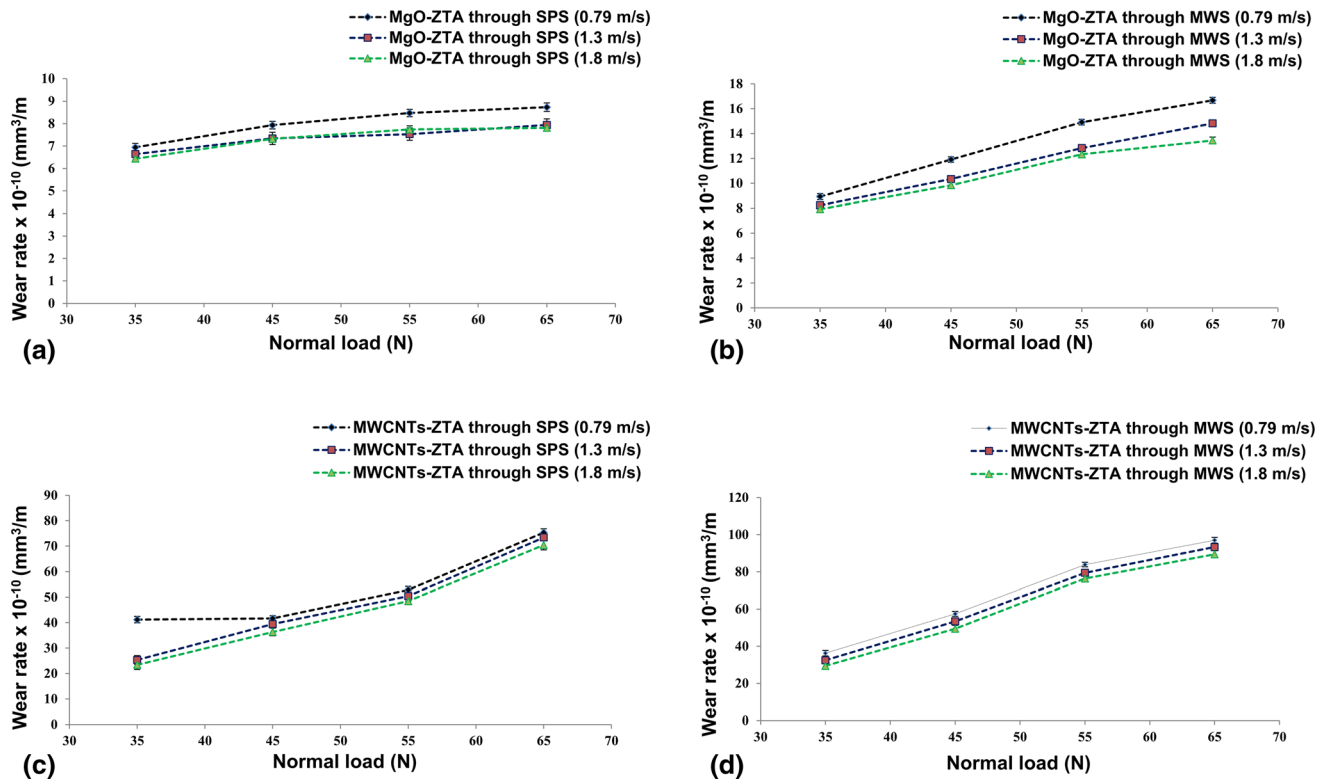


Fig. 5 Variations in the wear rate by varying normal load and sliding velocity of (a) MgO-ZTA through SPS, (b) MgO-ZTA through MWS, (c) MWCNT-ZTA through SPS and (d) MWCNT-ZTA through MWS

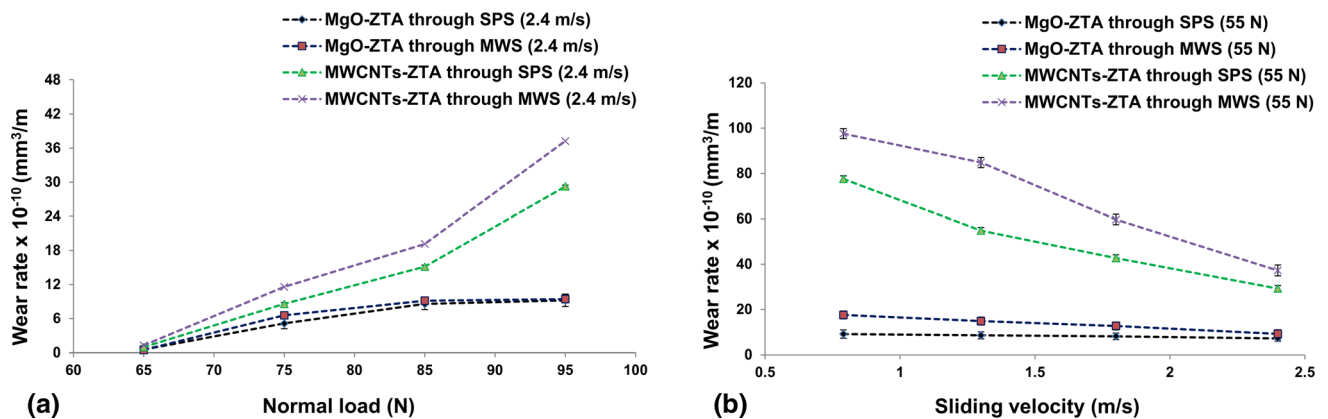


Fig. 6 Variations in wear rate with (a) variations in the normal load at a sliding velocity of 2.4 m/s, (b) varying sliding velocities along with constant normal load (55 N) of developed composites and comparisons between four samples

shown in Fig. 6(a). From Fig. 6(b), it can be seen that the wear rate of the composites decreased with an increase in the sliding velocity at a fixed load of 55 N. The variation in wear rate follows the same pattern as the COF. The SPS composites were found to have lower wear rate values compared to MWS composites. Among all the composites, the composites reinforced with MgO showed lower wear rates as compared to the composites reinforced with MWCNT as seen from Fig. 6(b).

The graph between COF versus sliding distance/time profile. Among the four developed composites, the graphs plotted of highest value of wear (MgO-ZTA through SPS) and minimum value of wear (MWCNT-ZTA through MWS) are shown in Fig. 7(a) and (b). From Fig. 7(a), it indicates that the COF occurs in three stages: (1) initial stage with an abrupt increase in

COF, when the sliding distance is around 16 s; (2) secondary stage of gradual increase in friction coefficient, occurring between 16 and 25 s; (3) steady and optimum friction stage, for the remaining sliding time. From Fig. 3(b), the COF profile with respect to the sliding distance was gradually increased and beyond almost constant after covering 1500 m of sliding distance under 65 N of constant normal loading with a constant sliding velocity of 2.4 m/s (Ref 53-55). The values of COF of MgO-ZTA through SPS higher than MWCNT-ZTA through MWS. Composites consolidated through SPS exhibited better tribological properties as compared to MW-sintered composites.

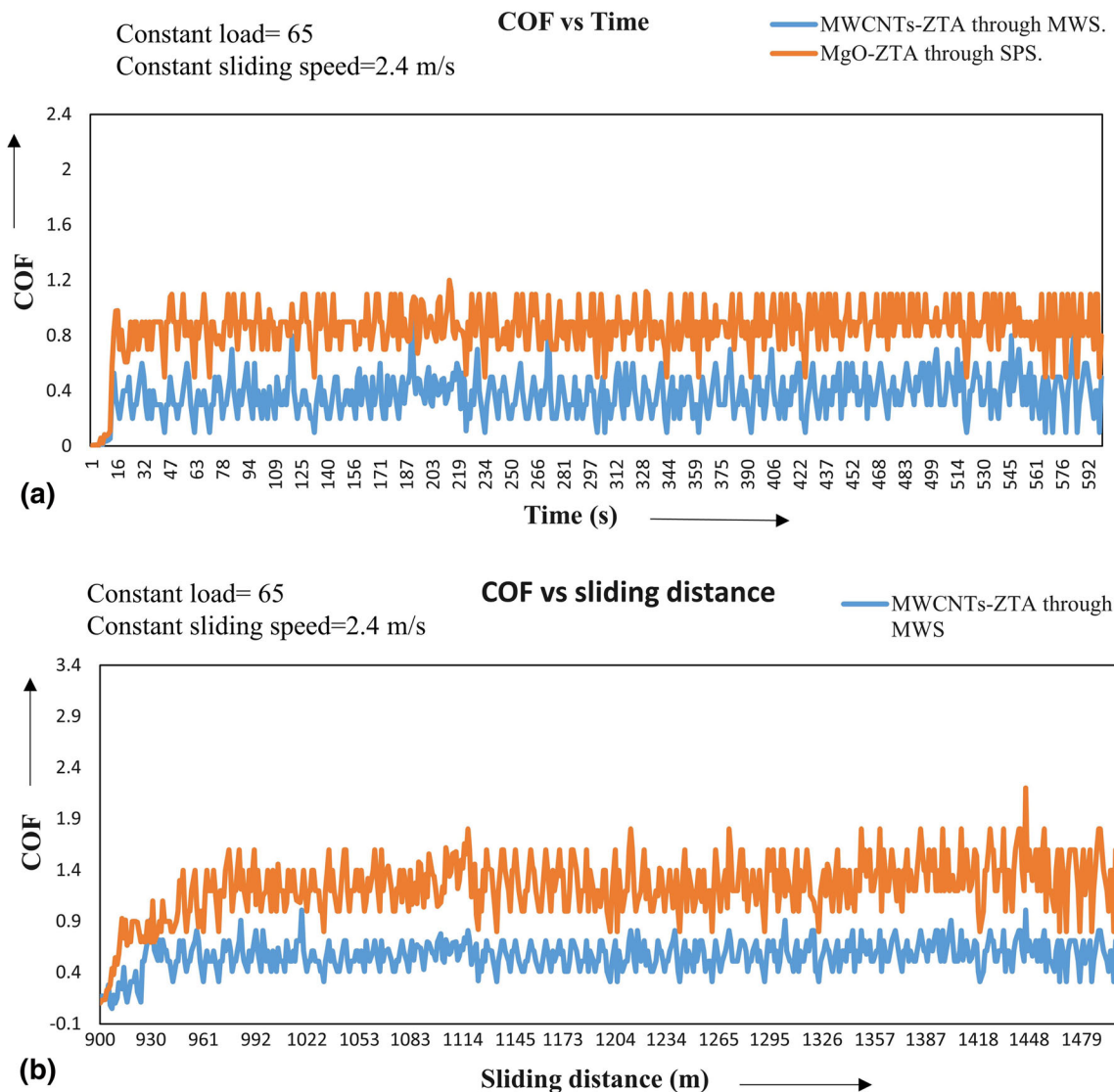


Fig. 7 (a) The graph plotted between COF versus time, (b) COF versus sliding distance at constant load (65) and constant sliding speed (2.4 m/s)

Figure 8 shows the FE-SEM microstructures of the surface of the composite sample pin, subjected to wear with 65 N as the normal load at a sliding velocity of 2.4 m/s.

During SPS process, superior rapid heating along with pressure was obtained as compared to MWS as discussed earlier. Due to the difference in sintering mechanisms, the average grain sizes obtained through SPS are lower compared to the grain sizes of MWS composites. Therefore, as a result of uniformly distributed grains and reduced grain sizes, composites sintered through SPS possess higher hardness. The MgO reinforcement also provided suppression of recrystallization and grain growth in the alumina matrix by forming a secondary phase resulting in increased hardness. On the other hand, the reinforcement of MWCNTs provided good fracture toughness but did not affect the hardness of the composites. Large pull-outs, broad and deep grooves were observed in the MWS composites due to wear as seen from Fig. 8(b) and (d). In the samples sintered through SPS, small pull-outs and fine grooves were observed as seen from Fig. 8(a). However, large pull-out, broad and fine deep grooves were found in the samples which

were reinforced with MWCNT and sintered through SPS as shown in Fig. 8(c). The tribo-layer is built up of layers by removing debris due to the rubbing action between the two contact parts during the tribological performance of the rolling/sliding contacts. On application of progressively increased applied normal load, a tribo-layer is formed on the pin by the debris due to the rubbing action between the disk and pin. However, the tribo-layer formed by reinforcement particles could not be stabilized under higher applied loads due to the formation of shear strain during higher loads. Moreover, this layer formed by the reinforced particles might get transferred to the matrix and lead to crack propagation on the pin surface due to delamination and breakdown, resulting in wear loss. The formation and breakdown of the tribo-layer in the SPS composites can be observed in Fig. 8(a) and (c), respectively.

Based on the microstructure and AFM results of the worn-out surfaces of the samples of worn surfaces, the mechanisms involved in wear are estimated. Figure 9(a) shows the AFM images revealing the topography of MgO-ZTA SPS composites after subsection of wear. Figure 10(a) shows the AFM images

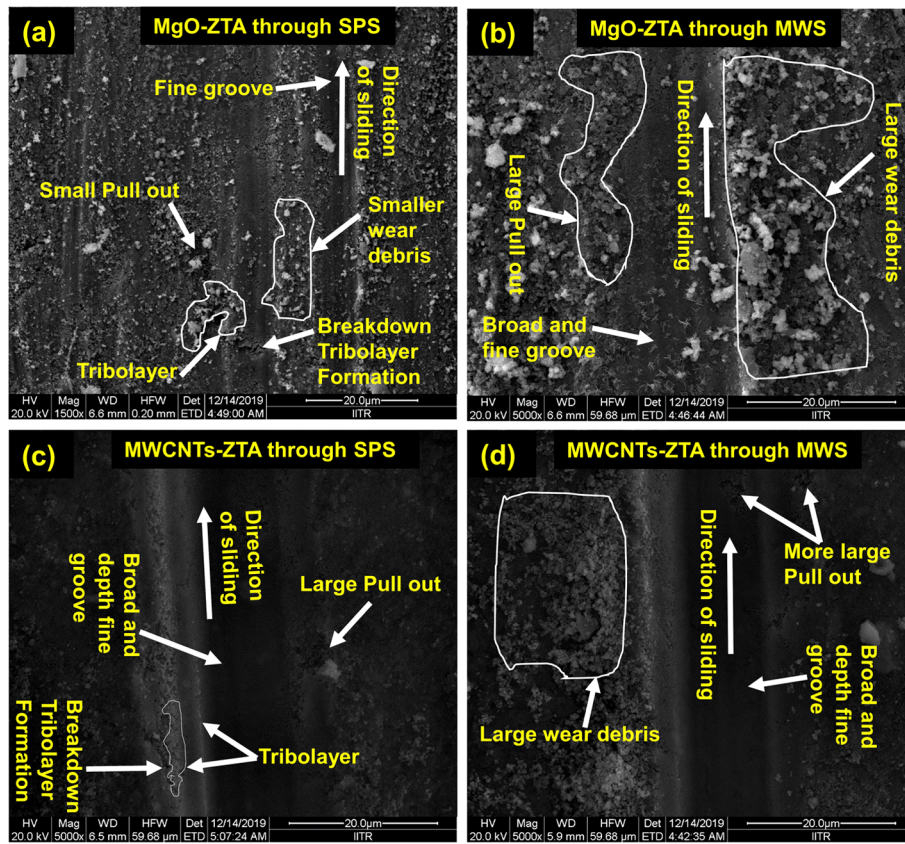


Fig. 8 FE-SEM microstructures of worn-out surfaces of the developed composite samples with a normal load of 65 N and a constant sliding velocity of 2.4 m/s of (a) MgO-ZTA composite developed through SPS, (b) MgO-ZTA composite developed through MWS, (c) MWCNT-ZTA composite developed through SPS, (d) MWCNT-ZTA composite developed through MWS

revealing the topography of MWCNT-ZTA MWS composites subjected to wear. The AFM topography of the wear surfaces of the SPS and MWS samples are shown in Fig. 9 and 10. Among the four different microstructure of composites shown in Fig. 8, the AFM results performed of highest value of wear are shown in Fig. 8(a) and composite with minimum value of wear is shown in Fig. 8(d), as discussed in previous sections.

From Fig. 9, it can be observed that the wear rate of the composites decreased with an increase in the sliding velocity at a fixed load of 55 N. The variation in the wear rate follows the same pattern as the COF. The SPS composites were found to have lower wear rate values compared to MWS composites. Among all the composites, the composites reinforced with MgO showed lower wear rates as compared to the composites reinforced with MWCNT as seen from Fig. 9 and 10 (Ref 45).

Figure 9(b) shows the 2D surface of the wear samples and the corresponding scars. Due to an increase in the normal loading, deep and steep grooves were formed on the surface due to sliding during wear and therefore exhibit maximum surface roughness with the highest peak ($h_{max} = 0.71 \mu\text{m}$) as seen from Fig. 9(c). Overall, the results reveal that all the composites exhibit a low volumetric wear rate with high COF. It can be observed from the topography that the width of the grooves on the surfaces does not vary much with an average surface roughness of $0.209 \mu\text{m}$ (Ref 56).

The AFM topography of the worn-out surface of MW-sintered MWCNT-ZTA composite subjected to wear with 65 N as the normal load is shown in Fig. 10. In the composites developed through MWS, the hardness of the MWCNT-ZTA is

higher as compared to MWCNT-ZTA composite, and therefore, the topography of their worn-out surfaces completely varies. A severer wear phenomenon was observed in the MW sintered MWCNT-ZTA composites as compared to the SP-sintered MgO-ZTA composites at the same sliding distance and normal loads. Figure 10(b) shows the worn-out surface of MW-sintered MWCNT-ZTA composite with a max height of the peak, h_{max} , and the average surface roughness 'Ra' as 1.05 and $0.659 \mu\text{m}$, respectively. The reason behind the occurrence of severe wear in this particular composite could be due to the decrease in the hardness of the composite, and at the same time rubbing between the surfaces, the actual contact area increases. On the other hand, at higher sliding velocities, the flow stress between the wear surface and the abrasive particles decreases, and hence, the abrasive indentation on the contact surface significantly increases resulting in an increase in the COF and indentation groove depth and width Fig. 10(c).

4. Conclusions

The following conclusions can be drawn from the present work:

1. Composites consolidated through SPS exhibited better densities as compared to MWS samples, although they also had reasonable relative densities.

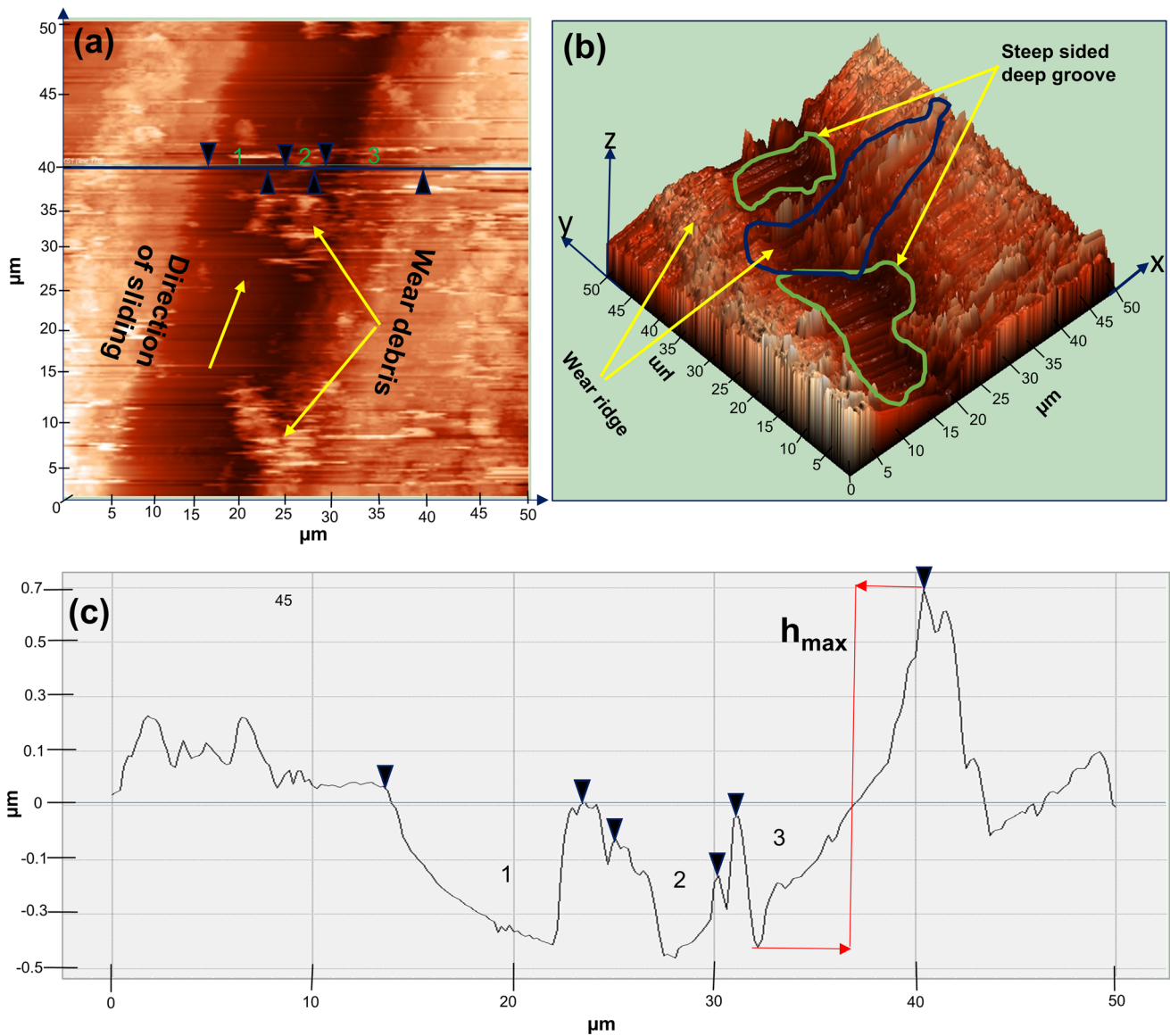


Fig. 9 The AFM results showing the worn surface profile with the inclined direction of MgO-ZTA through SPS at an applied load of 65 N and sliding distance 1500 m (a) 2D surface topography, (b) corresponding isometric 3D surface topography, (c) a line surface profile indicating the position of the line on (a)

2. Among the developed composites, the microhardness increased with the addition of MgO due to the promotion of the pinning effect. On the other hand, the addition of MWCNTs improved the fracture toughness by promoting crack branching.
3. Composites consolidated through SPS exhibited better tribological properties as compared to MW-sintered composites. However, in both cases, no compact tribo-layer formation was observed at lower normal load conditions and that might be the possible reason for the increase in the wear rate.
4. The composite's coefficient of friction (COF) and wear rate decrease and increase, respectively, with lower values (35N, 0.79 m/s) of wear parameter. The rate of wear also increases on the increase in normal load and sliding velocity. In comparison, the wear rate and COF increased on increase in normal loads (higher 95N) and sliding velocity under higher parameter values (1.8 m/s). The oxide tribo-layer formed breakdowns and underwent severe plastic deformation at a higher sliding velocity due to the effect of the flash temperature. However, at all sliding speeds, there is a rapid rise in the wear rate when normal load applied is beyond 65 N.
5. The COF values of MWS composites are comparatively higher than the SPS composites. This can be attributed to loosely bonded tribo-layer on top of the wear sample contact surface which undergoes severe wear during rubbing.
6. The rate of wear and COF values of the composites were obtained in the order as MgO-ZTA through SPS > MWCNT-ZTA through SPS > MgO-ZTA through MWS > MWCNT-ZTA through MWS.

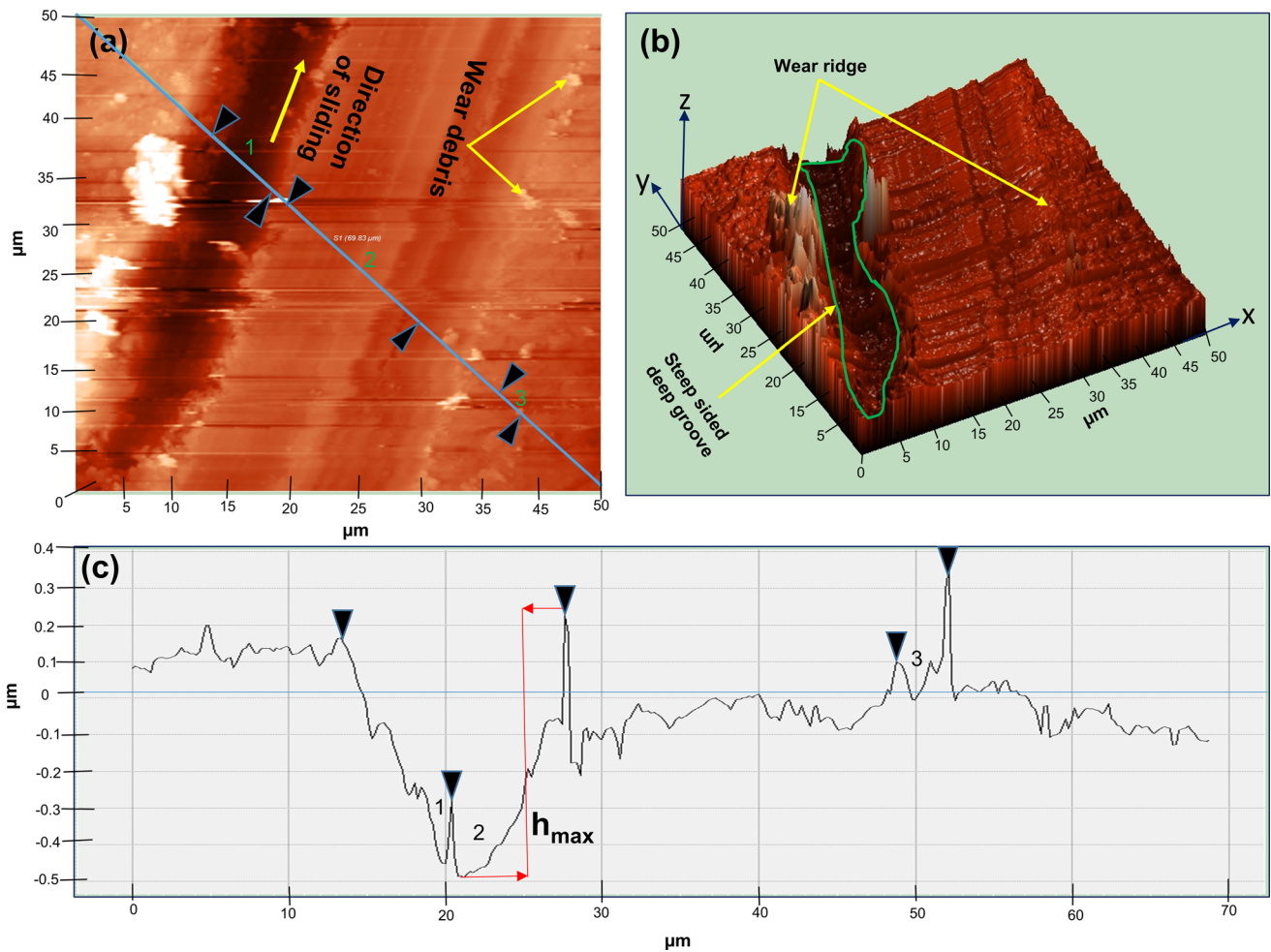


Fig. 10 AFM results showing the worn surface profile with x-axis direction of MWCNT-ZTA through MWS at an applied load of 65 N and sliding distance 1500 m (a) 2D surface topography, (b) corresponding isometric 3D surface topography, (c) line surface profile indicating the position of the line on (a)

Acknowledgments

The authors would like to thank the Ministry of Human Resources Department, Government of India, for providing monthly fellowship and the Indian Institute of Technology for providing necessary equipment and facilities.

Conflict of interest

The authors declare no conflict of interest.

References

1. K. Kato and K. Adachi, *Wear of Advanced Ceramics*, *Wear*, 2002, **253**, p 1097–1104
2. K. Kato, *Classification of Wear Mechanisms/Models*, *Proc. Inst. Mech. Eng. Part J J. Eng. Tribol.*, 2002, **216**, p 349–355
3. S. Mazumder, O.P. Kumar, D.K. Konekes and N. Mandal, *Tribological Influences of CuO into 3Y-TZP Ceramic Composite in Conformal Contact*, *J. Tribol.*, 2019, **141**(3), p 1–10. <https://doi.org/10.1115/1.4041894>
4. K.L. Meena and T.S. Srivatsan, *Influence of Sintering on the Development of Alumina-Toughened Nanocomposites: Conventional Versus Microwave. Metal-Matrix Composites: Advances in Analysis, Measurement, and Observations*, Springer, Berlin, 2021
5. K.L. Meena and D.B. Karunakar, *Development of Alumina Toughened Zirconia Nanocomposites Using Spark Plasma Sintering*, *Mater. Today Proc.*, 2018, **5**, p 16928–16935. <https://doi.org/10.1016/j.matpr.2018.04.096>
6. H.P. Cahoon and C.J. Christensen, *Sintering and Grain Growth of Alpha-Alumina*, *J. Am. Ceram. Soc.*, 1956, **39**, p 337–344. <https://doi.org/10.1111/j.1151-2916.1956.tb15599.x>
7. N. Claussen and J. Steeb, *Toughening of Ceramic Composites by Oriented Nucleation of Microcracks*, *J. Am. Ceram. Soc.*, 1976, **59**, p 457–458. <https://doi.org/10.1111/j.1151-2916.1976.tb09524.x>
8. R. Stevens, *Review Zirconia-Toughened Alumina (ZTA) Ceramics*, *J. Mater. Sci.*, 1989, **24**, p 3421–3440
9. A.K. Dey, S. Chatterjee and K. Biswas, *Effect of Oxide Additives on Phase Evolution and Tribological Behavior of Zirconia-Toughened Alumina Composite*, *J. Mater. Eng. Perform.*, 2017, **26**(12), p 6107–6116. <https://doi.org/10.1007/s11665-017-2851-z>
10. A.N. Krishnamurthy and R. Jain, *Wear Studies of Al₂O₃-ZrO₂-5CaO Composite Coatings for Tribological Applications*, *Int. J. Eng. Technol.*, 2018, **7**(3.4), p 73. <https://doi.org/10.14419/ijet.v7i3.4.16750>
11. M. Megahed, M.A. Attia, M. Abdelhameed and A.G. El-Shafei, *Tribological Characterization of Hybrid Metal Matrix Composites Processed by Powder Metallurgy*, *Acta Metall. Sin. (Engl. Lett.)*, 2017, **30**(8), p 781–790. <https://doi.org/10.1007/s40195-017-0568-5>
12. S. Mozammil, J. Karloopia, R. Verma and P.K. Jha, *Effect of Varying TiB₂ Reinforcement And Its Ageing Behaviour on Tensile and Hardness Properties of In-situ Al-4.5%Cu-xTiB₂ Composite*, *J. Alloys Compd.*, 2019, **793**, p 454–466
13. A. Al Mahmood, M.A. Gafur and M.E. Hoque, *Effect of MgO on the Physical, Mechanical and Microstructural Properties of ZTA-TiO₂*

- Composite, *Mater. Sci. Eng. A*, 2017, **707**, p 118–124. <https://doi.org/10.1016/j.msea.2017.09.048>
14. K.L. Meena and D.B. Karunakar, Effect of ZrO₂ and MgO Added in Alumina on the Physical and Mechanical Properties of Spark Plasma Sintered Nanocomposite, *Int. J. Refract. Met. Hard Mater.*, 2019, **81**, p 281–290. <https://doi.org/10.1016/j.jrmhm.2019.03.009>
 15. V. Sharma, M.L. Meena, M. Kumar and A. Patnaik, Waste Fly Ash Powder Filled Glass Fiber Reinforced Epoxy Composite: Physical, Mechanical, Thermo-mechanical, and Three-body Abrasive Wear Analysis, *Fibers and Polymers*, 2021, **22**, p 1–17
 16. M.L. Meena, G.S. Dangayach and A. Bhardwaj, An Ergonomic Approach to Design Hand Tool for Screen Textile Printing Handicraft Industry, *Int. J. Recent Adv. Mech. Eng.*, 2015, **4**(4), p 19–30
 17. B.K. Singh, H. Roy, B. Mondal, S.S. Roy and N. Mandal, Development and Machinability Evaluation of MgO doped Y-ZTA Ceramic Inserts for High-Speed Machining of Steel, *Mach. Sci. Technol.*, 2018, **22**(6), p 899–913. <https://doi.org/10.1080/10910344.2017.1415937>
 18. V. Chavan, S. Kadam and M. Sadaiah, Performance of Alumina-Based Ceramic Inserts in High-Speed Machining of Nimonic 80A, *Mater. Manuf. Proc.*, 2019, **34**(1), p 8–17. <https://doi.org/10.1080/10426914.2018.1532084>
 19. V. Sharma, M.L. Meena, M. Kumar and A. Patnaik, Mechanical and Three-Body Abrasive Wear Behavior Analysis of Glass and Basalt Fiber-Reinforced Epoxy Composites, *Polym. Compos.*, 2020, **41**(9), p 3717–3731
 20. Y.S. Wang, C. He, B.J. Hockey, P.I. Lacey and S.M. Hsu, Wear Transitions in Monolithic Alumina and Zirconia-Alumina Composites, *Wear*, 1995, **181–183**, p 156–164
 21. C.A.O. De Couto, S. Ribeiro and F.R. Passador, Effect of Carbon Nanotubes Reinforcement on the Mechanical Properties of Alumina and ZTA Composites for Ballistic Application, *Ceramica*, 2018, **64**(372), p 608–615. <https://doi.org/10.1590/0366-69132018643722475>
 22. A.Z.A. Azhar, H. Mohamad, M.M. Ratnam and Z.A. Ahmad, The Effects of MgO Addition on Microstructure, Mechanical Properties and Wear Performance of Zirconia-Toughened Alumina Cutting Inserts, *J. Alloys Compd.*, 2010, **497**(1–2), p 316–320. <https://doi.org/10.1016/j.jallcom.2010.03.054>
 23. F. Zhang, K. Vanmeensel, M. Inokoshi, M. Batuk, J. Hadermann, B. Van Meerbeek and J. Vleugels, Critical Influence of Alumina Content on the Low-Temperature Degradation of 2-3 mol.% Yttria-Stabilized TZP for Dental Restorations, *J. Eur. Ceram. Soc.*, 2015, **35**(2), p 741–750. <https://doi.org/10.1016/j.jeurceramsoc.2014.09.018>
 24. A. Rittidech, R. Somrit and T. Tunkasiri, Effect of Adding Y₂O₃ on Structural and Mechanical Properties of Al₂O₃-ZrO₂ Ceramics, *Ceram. Int.*, 2013, **39**, p S433–S436. <https://doi.org/10.1016/j.ceramint.2012.10.108>
 25. L. Melk, J. Josep, R. Rovira, M. Antti and M. Anglada, Coefficient of Friction and Wear Resistance of Zirconia-MWCNTs Composites, *Ceram. Int.*, 2015, **41**(1), p 459–468. <https://doi.org/10.1016/j.ceramint.2014.08.092>
 26. S. Mazumder and K.D. Kumar, Tribological Influences of CuO into 3Y-TZP Ceramic Composite in Conformal Contact, *J. Tribol.*, 2019, **141**, p 031606–10. <https://doi.org/10.1115/1.4041894>
 27. K. Ghosh, S. Mazumder, B.K. Singh, H. Hirani, P. Roy and N. Mandal, Tribological Property Investigation of Self-lubricating Molybdenum Based Zirconia Ceramic Composite Operational at Elevated Temperature, *J. Tribol.*, 2019, **142**, p 1–16. <https://doi.org/10.1115/1.4045015>
 28. Z. Dilshad, I. Sktani, N.A. Rejab, A. Fatah, Z. Rosli, A. Arab and Z.A. Ahmad, Effects of La₂O₃ Addition on the Microstructure Development and Physical Properties of Harder ZTA-CeO₂ Composites with Sustainable High Fracture Toughness, *J. Rare Earths*, 2020, **S1002–0721**(20), p 30294–30295. <https://doi.org/10.1016/j.jre.2020.06.005>
 29. M. Kuntz and R. Kruger, The Effect of Microstructure and Chromia Content on the Properties of Zirconia Toughened Alumina, *Ceram. Int.*, 2020, **44**(2), p 2011–2020. <https://doi.org/10.1016/j.ceramint.2017.10.146>
 30. I. Momohjimoh, M.A. Hussein and N. Al-Aqeeli, Recent Advances in the Processing and Properties of Alumina-CNT/SiC Nanocomposites, *Nanomaterials*, 2019, **9**, p 86
 31. A. Aaoulli, S. Bai, H.M. Cheng and J.B. Bai, Mechanical and Electrical Properties of a MWNT/Epoxy Composite, *Compos. Sci. Technol.*, 2002, **62**, p 1993–1998
 32. M.A. Awotunde, A.O. Adegbenjo, B.A. Obadele, M. Okoro, B.M. Shongwe and P.A. Olubambi, Influence of Sintering Methods on the Mechanical Properties of Aluminum Nanocomposites Reinforced with Carbonaceous Compounds: A Review, *J. Mater. Res. Technol.*, 2019, **8**(2), p 2432–2449. <https://doi.org/10.1016/j.jmrt.2019.01.026>
 33. U. Ta, V. Carle, U. Scha, M.J. Hoffmann, Preparation and Microstructural Analysis of High-Performance Ceramics, *Metallogr. Microstruct.*, **9**, 1057–1066 (2018). <https://doi.org/10.31399/asm.hba.v09.0003795>
 34. S. Ribeiro and F.R. Passador, Effect of Carbon Nanotubes Reinforcement on the Mechanical Properties of Alumina and ZTA Composites for Ballistic Application, *Ceramica*, 2018, **64**, p 608–615
 35. D. Sarkar, Preparation and Characterization of an Al₂O₃-ZrO₂ Nanocomposite, Part I: Powder Synthesis and Transformation Behavior During Fracture, *Compos. Part A Appl. Sci. Manuf.*, 2007, **38**, p 124–131. <https://doi.org/10.1016/j.compositesa.2006.01.005>
 36. M.A. Chowdhury, D.M. Nuruzzaman, A.H. Mia and M.L. Rahaman, Friction Coefficient of Different Material Pairs Under Different Normal Loads and Sliding Velocities, *Tribol. Ind.*, 2012, **34**(1), p 18–23
 37. R. West, *Anthony. Solid State Chemistry and Its Applications*, Wiley, New York, 2014
 38. P. Hagemuller, *Preparative Methods in Solid State Chemistry*, Elsevier, Amsterdam, 2012
 39. R. Sarkar, Phase Diagrams in the MgO-Al₂O₃ System, *IIC Bull.*, 2010, **20**, p 36–37
 40. Y. Zhang, Z.H. Guo, Z.Y. Han, X.Y. Xiao and C. Peng, Feasibility of Aluminum Recovery and MgAl₂O₄ Spinel Synthesis from Secondary Aluminum Dross, *Int. J. Miner. Metall. Mater.*, 2019, **26**(3), p 309–318
 41. T.J. Mroz, T.M. Hartnett, J.M. Wahl, L.M. Goldman, J. Kirsch, W.R. Lindberg, Recent Advances in Spinel Optical Ceramic. In: Window and Dome Technologies and Materials IX, *Int. Society for Optics and Photonics*, vol. 5786, pp. 64–70 (2005)
 42. S. Zhang and W.E. Lee, *Spinel-Containing Refractories*, *Mech. Eng.-New York and Basel-Marcel Dekker then CRC Press/Taylor and Francis*, 2004, **178**, p 215
 43. M. Kumar, M.A. Megalingam, V. Baskaran and K.S.H. Ramji, Effect of Sliding Distance on Dry Sliding Tribological Behaviour of Aluminum Hybrid Metal Matrix Composite (AlHMMC): An Alternate For Automobile Brake Rotor—A Grey Relational Approach, *J. Eng. Tribol.*, 2015, **230**(4), p 402–415
 44. S. Mozammil, E. Koshta and P.K. Jha, Abrasive Wear Investigation and Parametric Process Optimization of In situ Al–4.5% Cu–xTiB₂ Composites, *Trans. Ind. Inst. Met.*, 2021, **74**(3), p 629–648
 45. T. Holland, U. Anselmi-tamburini, D. Quach, T. Roehling and A. Mukherjee, Effect of local Joule heating during the Field-Assisted Sintering of Ionic Ceramics, *J. Eur. Ceram. Soc.*, 2012, **32**, p 3667–3674. <https://doi.org/10.1016/j.jeurceramsoc.2012.02.033>
 46. X.J. Zhang, Z.K. Dai, X.R. Liu, W.C. Yang, M. He and Z.R. Yang, Microstructural Characteristics and Mechanical Behavior of Spark Plasma-Sintered Cu–Cr–rGO Copper Matrix Composites, *Acta Metall. Sin. (Engl. Lett.)*, 2018, **31**, p 761–770
 47. L.K. Singh, A. Bhaduria, S. Jana and T. Laha, Effect of Sintering Temperature and Heating Rate on Crystallite Size, Densification Behaviour and Mechanical Properties of Al-MWCNT Nanocomposite Consolidated via Spark Plasma Sintering, *Acta Metall. Sin. (Engl. Lett.)*, 2018, **31**, p 1019–1030
 48. V. Naglieri, P. Palmero, L. Montanaro and J. Chevalier, Elaboration of Alumina-Zirconia Composites: Role of the Zirconia Content on the Microstructure and Mechanical Properties, *Materials*, 2013, **6**, p 2090–2102. <https://doi.org/10.3390/ma6052090>
 49. A.Z.A. Azhar, H. Mohamad, M.M. Ratnam and Z.A. Ahmad, Effect of MgO Particle Size on the Microstructure, Mechanical Properties and Wear Performance of ZTA-MgO Ceramic Cutting Inserts, *Int. J. Refract. Met. Hard Mater.*, 2011, **29**, p 456–461. <https://doi.org/10.1016/j.jrmhm.2011.02.002>
 50. M. Michalek, J. Sedlacek, M. Parchoviansky, M. Michalkova and D. Galusek, Mechanical Properties and Electrical Conductivity of Alumina/MWCNT and Alumina/Zirconia/MWCNT Composites, *Ceram. Int.*, 2014, **40**, p 1289–1295. <https://doi.org/10.1016/j.ceramint.2013.07.008>
 51. A. Ravikiran, G. Subbanna and B.P. Bai, Effect of Interface Layers Formed During Dry Sliding of Zirconia Toughened Alumina (ZTA) and Monolithic Alumina Against Steel, *Wear*, 1996, **192**(1), p 56–65

52. T. Senda, J. Drennan and R. McPherson, Sliding Wear of Oxide Ceramics at Elevated Temperatures, *J. Am. Ceram. Soc.*, 1995, **78**, p 3018–3024
53. K.L. Meena, C.S. Vidyasagar and D.B. Karunakar, Mechanical and Tribological Properties of Alumina Toughened Zirconia Composites through Conventional Sintering and Microwave Sintering, *Trans. Indian Inst. Metals*, 2020, **73**(7), p 1909–1923. <https://doi.org/10.1007/s12666-020-02001-y>
54. H. Fan, T. Hu, Y. Zhang, Y. Fang, J. Song and L. Hu, Tribological Properties of Micro-Textured Surfaces of ZTA Ceramic Nanocomposites Under the Combined Effect of Test Conditions and Environments, *Tribol. Int.*, 2014, **78**, p 134–141. <https://doi.org/10.1016/j.triboint.2014.05.010>
55. S. Mazumder, O.P. Kumar, D.K. Kotnees and N. Mandal, Tribological Influences of CuO Into 3Y-TZP Ceramic Composite in Conformal Contact, *J. Tribol.*, 2019 <https://doi.org/10.1115/1.4041894>
56. J.F. Bartolome, A. Smirnov, F. Sommer, R. Landfried and R. Gadow, Sliding Wear Behavior of ZTA with Different Yttria Stabilizer Content, *J. Am. Ceram. Soc.*, 2015, **98**(12), p 3981–3987. <https://doi.org/10.1111/jace.13795>

Publisher's Note Springer Nature remains neutral with regard to jurisdictional claims in published maps and institutional affiliations.